Soft Matter

Accepted Manuscript

This article can be cited before page numbers have been issued, to do this please use: M. A. Raoufi, S. Razavi Bazaz, H. Niazmand, O. Rouhi, M. Asadnia, A. Razmjou and M. Ebrahimi Warkiani, *Soft Matter*, 2020, DOI: 10.1039/C9SM02067E.

ROYAL SOCIETY OF CHEMISTRY

rsc.li/soft-matter-journal

View Article Online
DOI: 10.1039/C9SM02067E

Fabrication of unconventional inertial microfluidic channels using wax 3D printing

Mohammad Amin Raoufi[1,2,3], Sajad Razavi Bazaz[2], Hamid Niazmand[3], Omid Rouhi[1], Mohsen Asadnia[2], Amir Razmjou[4,5], and Majid Ebrahimi Warkiani [2, 6*]

[1] School of Biomedical Engineering, University of Technology Sydney, NSW, 2007, Australia

[2] School of Engineering, Macquarie University, NSW, 2109, Australia

[3]Department of Mechanical Engineering, Ferdowsi University of Mashhad, Mashhad, Iran

[4]Department of Biotechnology, Faculty of Advanced Sciences and Technologies, University of Isfahan, Isfahan 73441-81746, Iran

[5]UNESCO Centre for Membrane Science and Technology, School of Chemical Science and Engineering, University of New South Wales, Sydney, 2052, Australia

[6]Institute of Molecular Medicine, Sechenov First Moscow State University, Moscow 119991, Russia

***** Contact

Majid Ebrahimi Warkiani (majid.warkiani@uts.edu.au)

School of Biomedical Engineering, University Technology Sydney, Sydney, New South Wales 2007, Australia

View Article Online
DOI: 10.1039/C9SM02067E

Abstract:

Inertial microfluidics has emerged over the past decade as a powerful tool to accurately control cells and microparticles for diverse biological and medical applications. Many approaches have been proposed to date in order to increase the efficiency and accuracy of inertial microfluidic systems. However, the effects of channel cross-section and solution properties (Newtonian or non-Newtonian) have not been fully explored, primarily due to limitations in current microfabrication methods. In this study, we overcome many of these limitations using wax 3D printing technology and softlithograghy through a novel workflow, which eliminates the need for use of silicon lithography and polydimethylsiloxane (PDMS) bonding. We have shown that by adding dummy structures to reinforce the main channels, optimizing the gap between the dummy and main structures, and dissolving the support wax on a PDMS slab to minimize the additional handling steps, one can make various non-conventional microchannels. These substantially improve upon previous wax printed microfluidic devices where the working area falls into the realm of macrofluidics rather than microfluidics. Results revealed a surface roughness of 1.75 μm for the printed channels, which does not affect the performance of inertial microfluidic devices used in this study. Channels with complex cross-sections were fabricated and then analyzed to investigate the effects of viscoelasticity and superposition on the lateral migration of the particles. Finally, as a proof of concept, microcarriers were separated from human Mesenchymal Stem Cells using an optimized channel with maximum cell-holding capacity, demonstrating the suitability of these microchannels in the bioprocessing industry.

Keywords: *Wax 3D Printing; Inertial Microfluidics; Particle Separation; Computational fluid dynamics; Stem Cells*

View Article Online
DOI: 10.1039/C9SM02067E

1 Introduction

Microfluidics refers to the accurate control of flows and microparticles confined to the channels with micrometer dimensions. Overall, microfluidic systems can be categorized into active and passive based on the source of the force applied to the particles. Among passive systems, inertial microfluidics shows a great promise due to its high throughput, low cost, ease of fabrication, and automation. In these systems, particles of different sizes can be sorted using the inherent inertial lift and drag forces for use in biomedical and industrial applications[1]. This technique has several advantages over conventional particle sorting methods, including low sample volumes, high-throughput, low cost, and fast processing. Lateral migration of microparticles was first observed around 60 years ago [2], followed by several experimental and theoretical studies about the underlying physics [3-7]. This phenomenon was not widely employed by researchers until the availability of advanced microfabrication technologies enabled investigators to precisely fabricate microchannels with characteristic dimensions comparable to the microparticle/cell sizes. These advancements allowed researchers to fabricate microchannels of various shapes, including straight, spiral, serpentine, and expansion-contraction for a myriad of applications such as microfiltration [8, 9], droplet generation [10], flow cytometry [11, 12], fluid mixing [13, 14], and cell separation [15-18]. In addition to inertial forces in straight microchannels, secondary flows in curved channels or around obstacles give extra controllability to inertial microfluidics by applying an extra viscous drag force perpendicular to the main flow direction [19-22]. Secondary flows, wall induced forces, and shear gradient lift forces are strongly dependent on the channel size and geometry; hence, significant efforts have been made to produce complex microchannels, with the aim of improving particle focusing [23-27].

View Article Online
DOI: 10.1039/C9SM02067E

Microfluidic devices can be categorized into two groups based on the channels' connectivity and shape, namely two-dimensional (2D) (planar) and three-dimensional (3D) microdevices [28, 29]. In planar microfluidic systems, all the channels are arranged on a same plane regardless of their size, while 3D devices consist of non-planar channels and crossover features which form a more complex 3D structure. The SU8 photolithography technique is the most well-known patterning method to fabricate planar structures on silicon wafers [30]. In the past, many planar microchannels with rectangular and square cross-sections have been fabricated using the silicon softlithography technique to manipulate cells and microparticles within inertial microfluidic systems [11, 17, 31-35]. Although this approach has been the basis of many microfluidic device developments, some major drawbacks such as the requirement for expensive microfabrication equipment, skilled operators, and an inability to build non-planar structures impeded its widespread utilization [36, 37]. Silicon direct etching (wet or dry) [38, 39] and mechanical machining (i.e., micro-milling [40, 41]) are other options for producing 2D structures, mainly for non-rectangular cross-sections [42-44]. Using these approaches, multiple groups reported the fabrication of polydimethylsiloxane (PDMS)-made trapezoidal, circular, and triangular microchannels, resulting new insights into the physics of inertial microfluidics, and emergence of new applications of these devices [26, 45-47]. In addition, other techniques such as hot embossing [47, 48] and laser cutting [49-51] have been also used for fabrication of microchannels in glass and polymers; however, these approaches require sophisticated equipment, making them less viable options for rapid prototyping.

Lately, additive manufacturing (AM) or 3D printing has been extensively explored for fabrication of functional microfluidic devices (*i.e.,* micromixers, microvalves, and micropumps [52-54]), including microchannels from a variety of polymeric materials [55]. The ability of AM, especially stereolithography apparatus (SLA) for 3D printing of PDMS-based channels has also been

View Article Online
DOI: 10.1039/C9SM02067E

illustrated [56]. In 2014, Lee *et al.* used SLA to fabricate a 3D helical trapezoidal channel in order to separate antibody-functionalized magnetic nanoparticle clusters from *Escherichia coli* (EC) bacteria using a combination of Dean drag and inertial lift forces [57]. Following this, several SLA printers and resins have been developed each is capable of fabricating specific structures and features [56, 58, 59]. These developments aimed at eliminating the deficiencies of the previous approaches such as biocompatibility, printing resolution, and transparency [60, 61]. While modern SLA printers have overcome many of the previous problems, resolution of the small-size printed microchannels (~30 μm) is still insufficient for many of the inertial microfluidic applications. In addition, transparent-printed channels are in the milli and macro sizes, making their application restricted for inertial microfluidics. More recently, Sacrificial 3D printed molds have been used in fabrication of microfluidic devices, where PDMS elastomer has been cast into a wide range of dissolvable materials such as sugar alcohol isomalt [62], polyvinyl alcohol (PVA) [63], polyethylene glycol (PEG) [64], and acrylonitrile butadiene styrene (ABS) molds [65], and liquid metals [66]. Although the use of these materials is a step forward in simplifying the fabrication of microfluidic chips, some major drawbacks such as inadequate resolution of templates, distortion of PDMS microstructures, and presence of residual materials in channel networks limit their adaptation for inertial microfluidic applications [66]. In addition, the resolution of microchannels obtained using these template-assisted techniques is not high enough to meet the requirement of inertial microfluidics. Fused deposition modeling (FDM) 3D printing is a new method for making sacrificial molds for the fabrication of channels with non-conventional geometries [67]. Despite the capability of this method for fabrication of non-rectangular channels, the difficulty of modifying printing nozzles and the inferior surface quality of the resulting printed objects hinder its widespread adoption.

View Article Online
DOI: 10.1039/C9SM02067E

In order to address these issues, in this study, we report a new approach for the fabrication of PDMS microchannels using a wax 3D printer, enabling rapid prototyping of complex structures while avoiding solid-to-solid bonding. We have developed a new technique for fabrication of microchannels of arbitrary cross-sections by introducing dummy structures to support the main parts and dissolving the support wax on a PDMS slab to minimize the additional handling steps. Various straight and curvilinear microchannels have been fabricated using our proposed methodology. Then, focusing of micron-size particles at different flow rates was observed and analysed for both Newtonian and viscoelastic fluids to demonstrate the suitability of the printed microchannel for inertial microfluidic applications. Finally, separation of stem cells from microcarriers was demonstrated in a novel wax printed spiral channel, showcasing the suitability of this technique for the bioprocessing industry.

2 Materials and methods

2.1 Design and fabrication process

Fig. 1 shows all steps from design to casting of the microfluidic channels via the wax 3D printing method. As per the workflow presented in Fig.1A, SolidWorks 2016 software (Dassault Systemes SolidWorks Corporation, Waltham, MA, USA) was first used to design the channels (Fig. 1A Ⅰ). At this step, it is vital to design specific dummy structures to prevent breakage/collapse of microchannels during the post-processing steps, as the main channels are extremely fragile. Fig. 1A Ⅰ shows a single-curved microchannel reinforced by a dummy structure in the center. Although the dummy structure is not connected to the main channel, it prevents the main channel from breakage during the peel-off step because the design is printed as a single block comprising two structures (the main channel and the dummy structure printed by castable wax) connected together by the support wax (Fig. 1B ⅠI). It should be noted that the dummy structure needs to be

View Article Online
DOI: 10.1039/C9SM02067E

symmetrical and separate from the main channel to prevent distortion and to allow easy disconnection from the main channel during removal of the support wax. The gap between the main channel and the dummy structure should be selected carefully, as large gaps can prevent the structure from being printed homogenously, causing the channel to collapse during the peel-off process, while minute gaps can lead to unwanted adhesion between the dummy and main structures. We found that the optimum gap between the dummy and main structures is 250-500 μm. The gap is intended to be filled with support wax during the printing step, resulting in a homogenous structure. Material of the dummy structure is the same as the main channel (Midas Castable Material) and resistive to BIOACT VSO solvent. In the design step, the dummy structures and main channels should be designed together to be printed at the same time during the printing step. Thickness of the dummy structures in all designs is 2 mm to make the printed object stronger, handling steps more straightforward, and prevent the channel breakage during the peel-off. In high-aspect-ratio straight channels, the dummy structure needs to be symmetrical to prevent any distortion after the support wax removal. In practical applications, microchannels are symmetrical and dummy structures can be easily designed to form a symmetrical structure. Curve channels or structures with non-symmetrical shapes tolerate the thermal distortion due to the curvature of the design. Therefore, in these channels, the symmetry of the dummy structure is not a critical issue. In these structures, the entire design can be hypothetically divided into some pieces, and different dummy structures can be used to support each part. In Fig. 1B Ⅰ I, only the dummy structure (in blue) and the support wax (in red) are visible, whereas the main microchannel is covered by support wax.

Following the design modeling, these models were saved as a stereolithography file (.STL) and exported to Modelwork and Analyzer software (Solidscape, Inc., USA) for further

View Article Online
DOI: 10.1039/C9SM02067E

modification. In the next step, the wax printer machine (Solidscape S350- Solidscape, Inc., USA) printed the complete structure layer by layer (Fig. 1A II, and 1B I) using additive and subtractive manufacturing. Each layer is generated by depositing droplets of molten wax, followed by a cooling process for solidification. At the end of each layer, a cutter trims back the structure surface for the next layer to be printed. The machine works with two different types of wax including Midas Castable Material (Solidscape, Inc., USA) to create the main structure, and Melt Dissolvable wax (Solidscape, Inc., USA) to support all the undercuts and overhangs during the fabrication process. Various layers of support wax can be printed beneath the main structure on the build plate to protect the main channel. Since inertial microfluidic channels are extremely fragile, at least 30 layers of support wax are essential to prevent them from any damage during the peel-off process. Once the part has been printed, it can be easily detached from the build plate by placing the plate onto a hot plate for 30 min at 55 °C, then sliding a thin nylon wire under the part. After the detachment of the printed structure from the build plate, it needs to be immersed in a BIOACT VSO (Vantage Specialty Chemicals, USA) solvent at 55 °C for 30 minutes to remove and dissolve the support wax (Fig. 1B III, and 1A III). The maximum temperature must be set to 55 °C, as higher temperatures can deform the structure. The VSO solvent only dissolves the support wax and is chemically unreactive Material of the dummy structure is the same as the main channel (Midas Castable Material) and resistive to BIOACT VSO solvent. In the design step, the dummy structures and main channels should be designed together to be printed at the same time during the printing step. Thickness of the dummy structures in all designs is 2 mm to make the printed object stronger, handling steps easier, and prevent the channel breakage during the peel-off. In high-aspect-ratio straight channels, the dummy structure needs to be symmetrical to prevent any distortion after the support wax removal. In practical applications, microchannels are symmetrical

View Article Online
DOI: 10.1039/C9SM02067E

and dummy structures can be easily designed to form a symmetrical structure. Curve channels or structures with non-symmetrical shapes tolerate the thermal distortion due to the curvature of the design. Therefore, in these channels, the symmetry of dummy structure is not a critical issue. In these structures, the entire desinge can hypothetically divided into some pieces, and different dummy structures can be used to support each part. We have added the mentioned description in the manuscript. to with castable counterparts. Dissolving the support wax must be performed on a cured PDMS (Sylgard 184 Silicone Elastomer Kit, Dow Corning, MI, USA) substrate in order to support the final structure, eliminating the need for manual handling of parts after the removal of support wax (Fig. 1B IV). When the support wax is completely dissolved, the detached dummy structures and the solvent are removed from the PDMS substrate by tilting the dish. Residuals are also cleaned by gently rinsing the structure with a clean and warm BIOACT solvent using a syringe. The rinsing continues until all debris and residuals are removed from the channel (Fig. 1B V and VI). After the mold fabrication, a degassed mixture of 10:1 PDMS and curing agent was poured over the 3D wax structure and cured in an oven at 55 ° C for 5 hours (Fig. 1B VII, and 1A IV). The cured PDMS was punched using a Uni-Core™ Puncher (Sigma-17 Aldrich Co. LLC, SG) at the inlet and outlet of the channels for fluidic access and wax cleaning. Finally, the 3D printed mold was removed from the PDMS by melting the wax in an oven (Fig. 1B VIII, and 1A V) at a temperature of 100–115 °C and flushing the channels with acetone at room temperature (Fig. 1B IX, and 1A VI). Using this approach eliminates the time-consuming PDMS bonding step and prevents the leakage at high flow rates since PDMS layers merge together during the curing process. It has been proven that acetone has negligible effects on the PDMS-made channels and can be used to clean the channels without damaging the device and altering its properties [68].

View Article Online
DOI: 10.1039/C9SM02067E

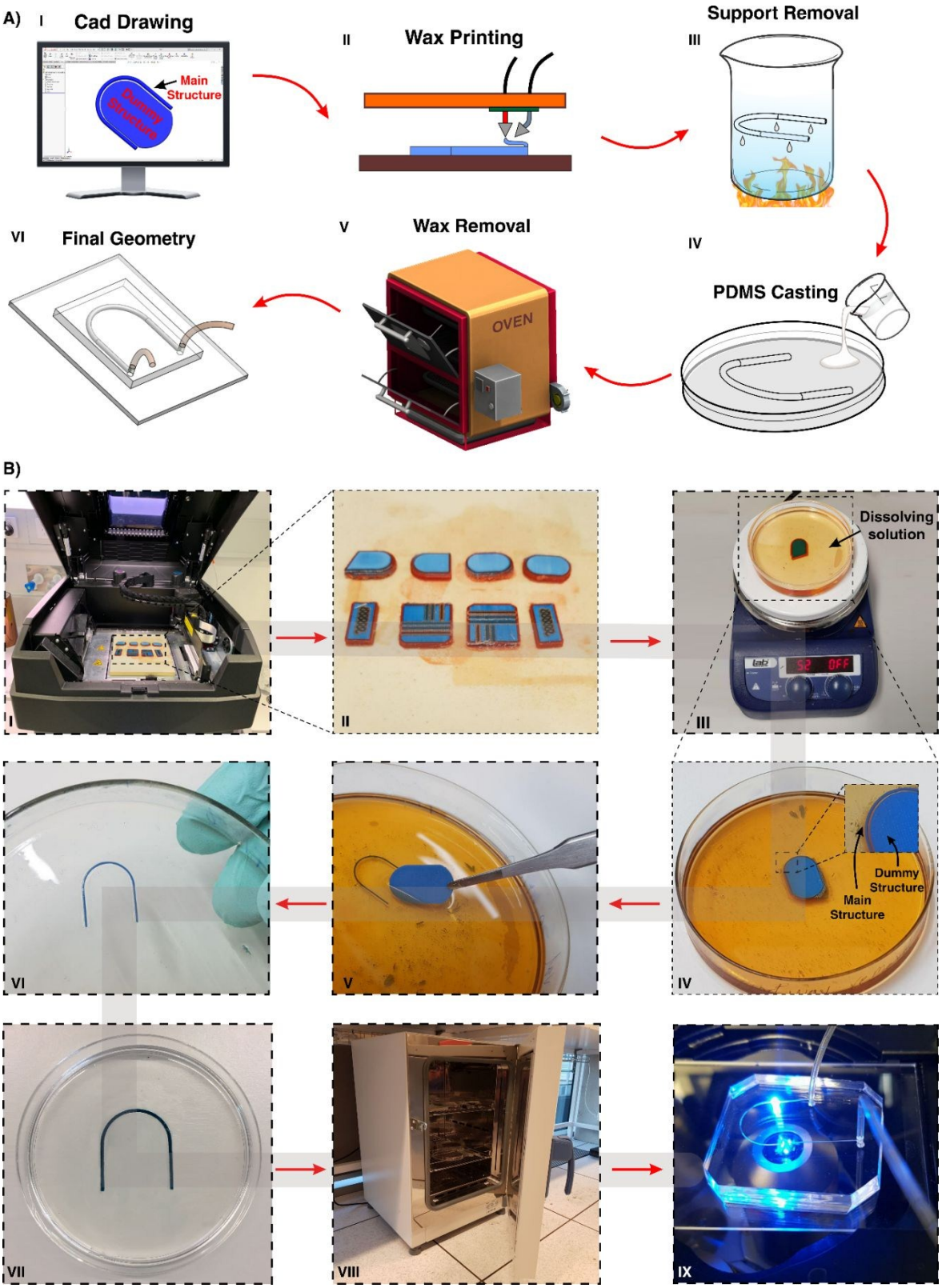

Fig. 1 Microchannel fabrication process by the wax printing approach. A) Schematic illustration of the proposed workflow for the fabrication of microchannels. A I) Channels design using CAD

View Article Online
DOI: 10.1039/C9SM02067E

software. A II) and B Ⅰ). Printing models with the wax 3D printer. The main microchannel is supported by the blue dummy structure in the middle and is covered by the supporting wax. The large dummy structure in the middle serves to protect the main channel from breaking during post-processing. B Ⅰ Ⅰ) Fabricated channels on the build plate which are placed on a hot plate for detachment. A III), and B III) Dissolving the support wax by immersing the chip in the BIOACT VSO solvent on a hot plate. B IV) Dissolution of the support wax (red) causes the main microchannel to appear gradually. The channel rests on a thin PDMS slab once the support wax was completely dissolved. B V) Dummy structure removal by tweezers. B VI) Cleaning the PDMS slab with new solvent and drying. A IV), and B VII) Pouring uncured PDMS on the fabricated wax channel. A V), and B VIII) Punching the cured PDMS at the inlet and outlet, and put it in the oven at a temperature of 115 °C. A VI), and B IX) The final microchannel after flushing the melted wax, and cleaning the channel with Acetone.

2.2 Experimental setup

In this experiment, all images were captured using an inverted epi-fluorescence microscope (Nikon Eclipse Ti) equipped with a monochrome CCD camera (NIKON DS-Qi1Mc) and a CoolLED pE300. The exposure time and long-working-distance objective were set to 400 ms and 4X, respectively. A high-speed camera (Phantom- VEO 640L) with 7000 fpm and 60 µs exposure time was used to take the images of microcarrier separation from stem cells. Fluorescent microbead (phosphorex-USA) suspensions (5×10^4 per mL) were loaded in 10 mL BD plastic syringes with Luer-Lok® tips and pumped through the microchannels using a Nexus 3000 syringe pump. In addition, the mixture of Dry Cytodex 3 microcarriers (GE Healthcare, the volume fraction of 0.15%) and stem cells (fat-derived hMSCs, the average concentration of 0.6×10^5 cells/mL) was driven continuously through the microchannels by a peristaltic pump (Shenchen, LabV1, China). Fat-derived hMSCs were first cultured in a T175 tissue culture flask in a humidified incubator at 37 °C and 5% CO_2 and then passaged in a high-glucose Dulbecco's modified Eagle's medium (DMEM, Life Technologies) supplemented with 1% Penicillin-Streptomycin (10,000 U/mL, Life Technologies Holdings Pte Ltd), 10 ng/mL bFGF (Sigma-Aldrich) and 10% fetal bovine serum (FBS, Life Technologies). After 80% confluency, they were washed with Mg^{2+} and Ca^{2+} free DPBS and dissociated by 25% trypsin and 0.53 mM EDTA. Finally, cells were suspended in the

View Article Online
DOI: 10.1039/C9SM02067E

five-fold diluted culture medium to neutralize the trypsin, harvested by centrifugation, and re-suspended in the culture medium with desired cell concentration. Microcarriers were hydrated by 1X, Mg^{2+} and Ca^{2+} free phosphate buffer saline (PBS) for three hours, and then washed by PBS before autoclaving. Finally, the microcarriers were stocked and suspended with the volume fraction of 0.15%.

In order to make a Newtonian sample, 100 µL of fluorescein (green) was diluted in 15 mL of Auto MACS buffer (Miltenyi Biotec). The viscoelastic solution was also made by adding 0.1 g of polyethylene oxide (PEO, Sigma-Aldrich, Mw = 2000 kDa) powder to 50 mL of AutoMACS buffer solution. In order to measure the viscoelasticity of the PEO solution, relaxation time (λ) and viscosity of the PEO solution (η_p) were measured by a capillary breakup extensional rheometer (CaBER-1, ThermoHakke) and a rotational rheometer (MCR-301, Anton Paar), respectively, as λ_{mean}= 0.0106 s and η_p=0.031. All the solutions and tests were made and performed at room temperature (27 °C). It should be noted that peristaltic pumps produced some small pulsation; however, as we used a pressure damper, and given the flexibility of PDMS-made channels, this had no effect on the flow profile and particle focusing.

2.3 Surface characterization

The surface of the PDMS device replicated from the wax printed mold was examined by a 3D laser microscope (Olympus LEXT OLS5000) with an LMPLFLN 10x LEXT objective lens (Olympus). Profilometry images were used to analyze the surface morphology, surface roughness, and step heights. The surface roughness was evaluated as arithmetical mean height (Sa), which measures the average magnitude of variation in the height of individual points, compared with the arithmetical mean of the corresponding surface [69].

View Article Online
DOI: 10.1039/C9SM02067E

3 Results and discussion:

3.1 Wax 3D printer

The nominal resolution of the S350 Wax 3D printer used in this study is 6 μm in the Z axis (layer thickness) and 24 μm in the X and Y axes. Nevertheless, based on our findings, the smallest printable dimension for rectangular cross-section is approximately 75 μm in width and 50 μm in height (hydraulic diameter ~ 60 μm), whereas for non-rectangular geometries this value increases to 200 μm. We decided to fabricate different channels with 250 μm hydraulic diameter in order to evaluate the printing quality for different geometries and to compare the effect of channel cross-sectional geometry on particle migration under similar hydrodynamic conditions.

3.2 Characterization of microfluidic devices

The surface finish of PDMS replica and its performance strongly depend on the fabrication procedure [36]. Conventional soft lithography techniques using microfabricated molds are not able to produce microchannels with non-planar cross-sections (e.g., triangular, circular), especially in curvilinear geometries. In addition, bonding a PDMS slab to another PDMS layer or a glass slide requires tedious micro-scale alignment and surface treatments (oxygen plasma, adhesive, ultrasonic, etc.), all of which can result in leakage at the interface of two surfaces. Here, we have proposed a new methodology based on the wax 3D printing and soft lithography capable of overcoming mentioned issues. To this end, we fabricated straight, curved, and spiral microchannels with different cross-sections (i.e., circular, rectangular, triangular and complex) as shown in Fig. 2A and 2C. Careful characterization of fabricated microchannels using this approach revealed that all geometries have a good surface finish with Sa of ~ 1.75 μm (Fig. 2B) and are close to the designed structures dimensionally (errors of less than 3%). To better illustrate the quality of the fabricated channels, a magnified view of the triangular channel is presented. As can

View Article Online
DOI: 10.1039/C9SM02067E

be seen, while the fabrication workflow precisely makes the sharp edges, the triangular tip was printed imperfectly due to the printing resolution and geometrical constrains in X-Y directions. The required time for printing can vary as a function of channel size and the resolution value in the Z direction. For the objects printed in this study with 6 μm Z resolution, the time required was around 6 hr. It should be noted that the transparency of the final microchannels is comparable with that of PDMS, as the printed wax channels were used only as a sacrificial template for the PDMS casting. To the best of our knowledge, inertial focusing in curved circular and triangular microchannels has not been studied previously due to the difficulty of their microfabrication using conventional techniques. More importantly, the utilization of dummy structures proposed in this study (i.e., to reinforce the main channels during the peel-off from the print bed) allowed us to create high-quality microchannels, not reported in the previous studies [13, 68, 70]. Fig. 2C demonstrates cross-sections of different curved and straight microchannels fabricated by the wax printing method, which was further used for particle migration analysis in Newtonian and non-Newtonian solutions. All single curved channels (triangular, rectangular and circular cross-sections) share the same hydraulic diameter of 250 μm and curvature radius of 6.5 mm, for consistency of hydrodynamic conditions in each channel.

View Article Online
DOI: 10.1039/C9SM02067E

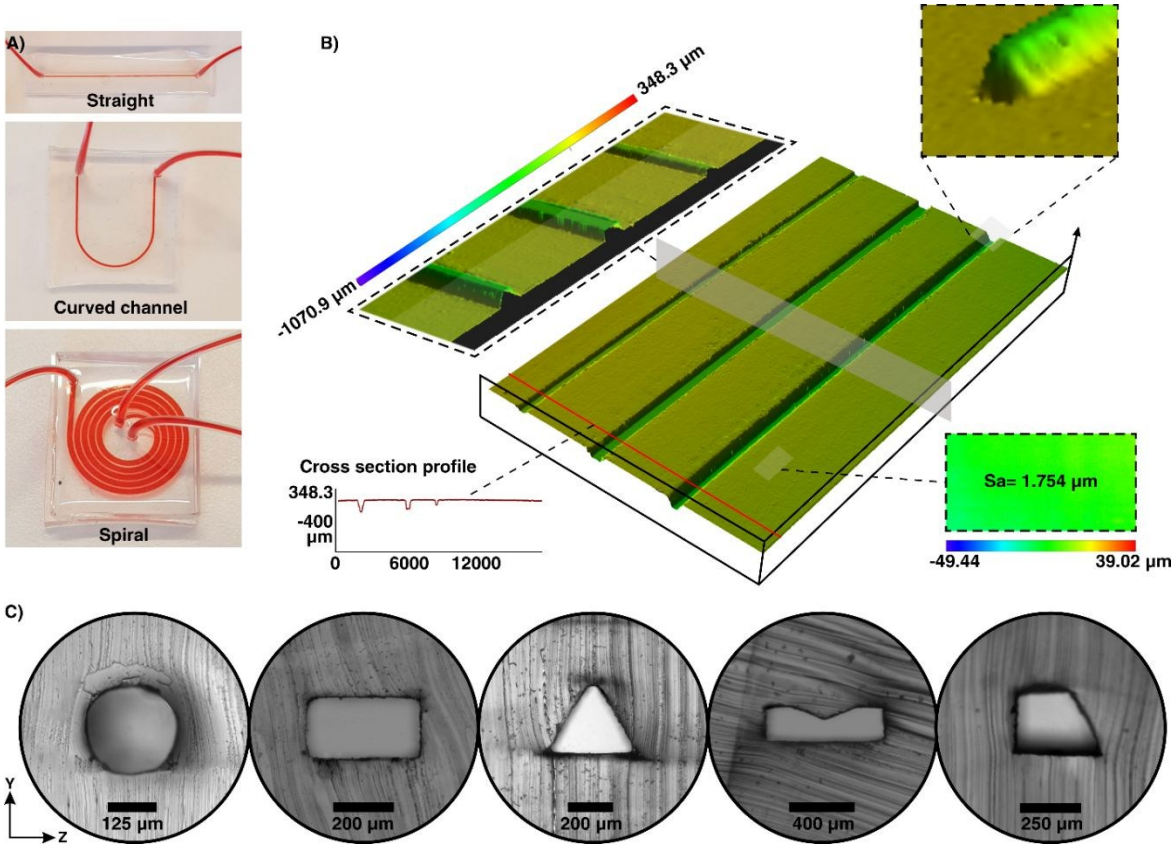

Fig. 2 A) Top view images of the PDMS devices used for particle sorting. B) Characterization of the wax printed channels using a profilometer device. It shows the printed channels from different angles, and surface roughness (1.75 µm). C) Cross-sectional optical micrograph of the PDMS microfluidic chips.

3.3 Numerical Simulation Results

In order to study the effects of channel geometry on the flow field and Dean vortices, three different circular, triangular, and rectangular curved channels with the same hydraulic diameter were numerically modeled in Comsol 5.3a, a commercially available software based on finite element method. For this purpose, the continuity and Navier Stokes equations for a laminar incompressible Newtonian flow were solved as follows:

$$\nabla . V = 0 \tag{1}$$

$$\rho(\frac{\partial V}{\partial t} + (V.\nabla)V) = -\nabla P + \mu\nabla^2 V \tag{2}$$

View Article Online
DOI: 10.1039/C9SM02067E

where P is the static pressure, V is the velocity vector, ρ is the fluid density, and μ is the dynamic viscosity of the fluid. For the Newtonian solution, ρ and μ were considered to be 998.2kg/m^3 and 0.001002 kgm^{-1}s^{-1}, respectively. As shown in Fig. 3, the curvature at the start of the bend in the channel acts as an obstacle and pushes the flow towards the inner wall. However, shortly after this, the flow shifts towards the outer wall and returns circumferentially to the inner wall, due to the presence of a centrifugal force caused by the curvature. These secondary flows, or Dean vortices, push the main flow outward and cause the velocity profile peak to occur near the outer wall. However, due to the changes in geometry, the maximum value of the velocity in each cross-section differs from the corresponding value in the other geometries. While the maximum velocity in the triangular channel is approximately 0.91 m/s, it drops to around 0.86 m/s in the circular and rectangular channels. Also, each channel has its range of helicity (defined in Eq. (3)), based on its shape. Helicity is the strength of Dean vortices in helical flows and is a practical variable to quantitatively evaluate secondary flows in curved channels, as a high value of helicity implies stronger Dean vortices and consequently more mixing [71].

$$H = \omega . \upsilon \tag{3}$$

where H is the helicity, and ω and υ indicate the angular and axial velocity, respectively.

As shown in Fig. 3, the rectangular geometry has a lower value of maximum helicity (≈ 400) compared to other channels (≈ 600), at the same flow rate. Thus, for high-throughput applications in spiral and curved channels where Dean drag is dominant compared to the other inertial forces, the rectangular geometry would be used in preference to the other cross-sections.

View Article Online
DOI: 10.1039/C9SM02067E

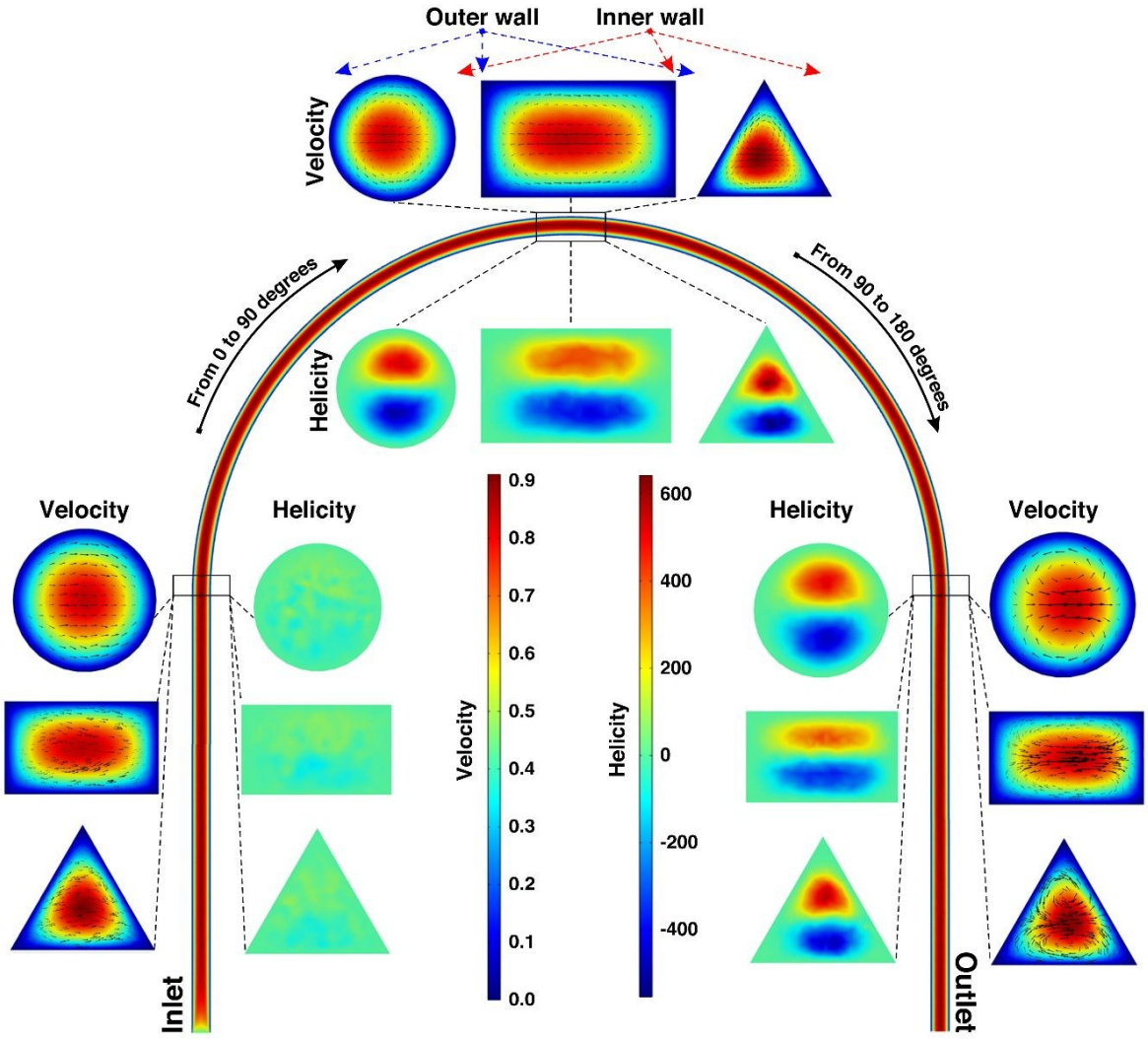

Fig. 3 Velocity and helicity contours for circular, rectangular, and triangular single curved channels for the flow rate of 1.1 ml/min. Through the curved section, the maximum velocity region gradually moves towards the outer wall. Rectangular and triangular channels have the least and most helicity, respectively.

Fig. 3 also shows that the location of the maximum helicity regions varies in each channel, noticeably altering the focusing positions in each channel. Generally, particle focusing happens in the regions where secondary flow drag is weak and can be balanced by inertial forces. At high flow rates, Dean vortices dominate the other inertial forces, and particles remain scattered throughout the channel [72].

View Article Online
DOI: 10.1039/C9SM02067E

3.4 Experimental Results

This section consists of three parts. First, we demonstrated the particle migration in a single curve channel with various cross-sections. Second, the particle behavior inside a straight channel with trapezoidal and complex cross-sections (a superposition of two trapezoids) was evaluated. Finally, as a proof of concept, we investigated using an optimized channel design for separation of human mesenchymal stem cells (hMSCs) (Regeneus Ltd, Australia) from microcarriers.

3.4.1 Curved Channels

During the last decade, curved and spiral channels have been extensively used to separate cells and particles (e.g., cancer cells, bacteria, and algae) from complex biofluid solutions [1]. As a result, finding a new method to fabricate curved channels with better separation efficiency is of great importance. In this part, focusing of 50 μm fluorescent particles is investigated for a wide range of flow rates in order to evaluate the functionality of the proposed fabrication method for inertial microfluidic applications.

In general, particle focusing in microchannels occurs when the diameter of flowing particles (a) is comparable to the characteristic length of the channel (D_H) ($a/D_H > 0.07$) [73]. Furthermore, for an appropriate value of blockage ratio ($a/D_H \approx 0.2$), focusing can occur even in a single-curved channel [74]. Typically, inertial forces can be divided into four categories, namely, wall-induced (F_w), shear gradient (F_s), Magnus (F_Ω), and elastic lift (F_E) forces. F_w is a repulsive force which pushes the particles away from the walls, while F_s acts in the opposite direction and forces the particles towards the walls. The Magnus force originates from the particle rotation and is due to the asymmetric shear stress on the particles. It causes particles to migrate circumferentially towards final equilibrium positions and only becomes significant wherever F_w and F_s substantially balance each other [75]. The viscoelastic force (F_E), arising from the non-Newtonian behavior of the

View Article Online
DOI: 10.1039/C9SM02067E

solution, pushes the particles towards the low shear stress regions. As shown in Fig. 4A, since the blockage ratio meets the criterion for single curve focusing (a/H = 0.2), particles can be focused in all of the curved channels. While all these channels have the same hydraulic diameter of 250 μm, due to the nonlinearity of their shapes, each channel has its own focusing behavior. As can be seen, for a Newtonian solution, particles focus close to the inner wall, where the secondary flow drag and inertial lift forces balance each other for a wide range of flow rates and all the cross-sections used. However, the focusing band and position vary between cross-sections. The triangular structure has the highest helicity value (based on numerical results in section 3.3); nevertheless, the particles are mainly concentrated in the center of the channel due to the presence of sharp corners and strong wall-induced lift forces towards the channel center. On the other hand, the additional elastic force arising from the non-Newtonian property of the PEO solution pushes the particles away from the inner wall and causes a new focusing position to form near the outer wall due to the synergistic effect of Dean drag and elastic forces (Fig. 4B). Near the outer wall, the outward Dean and shear gradient lift forces are balanced by the opposing wall-induced and elastic lift forces, resulting in particles reaching an equilibrium at this position. Fig. 4A also shows that for the non-Newtonian solution at a flow rate of 0.5 ml/min, particle migration towards the outer wall happens more gradually, since secondary flows are weaker in the rectangular channel than for the other channel geometries. Besides, it can be observed from the same figure that in the non-Newtonian solution, the focusing position of particles did not change for varying flow rates in circular and triangular cross-sections; However, in rectangular channels, higher flow rates resulted in the focusing band moving closer to the outer wall.

View Article Online
DOI: 10.1039/C9SM02067E

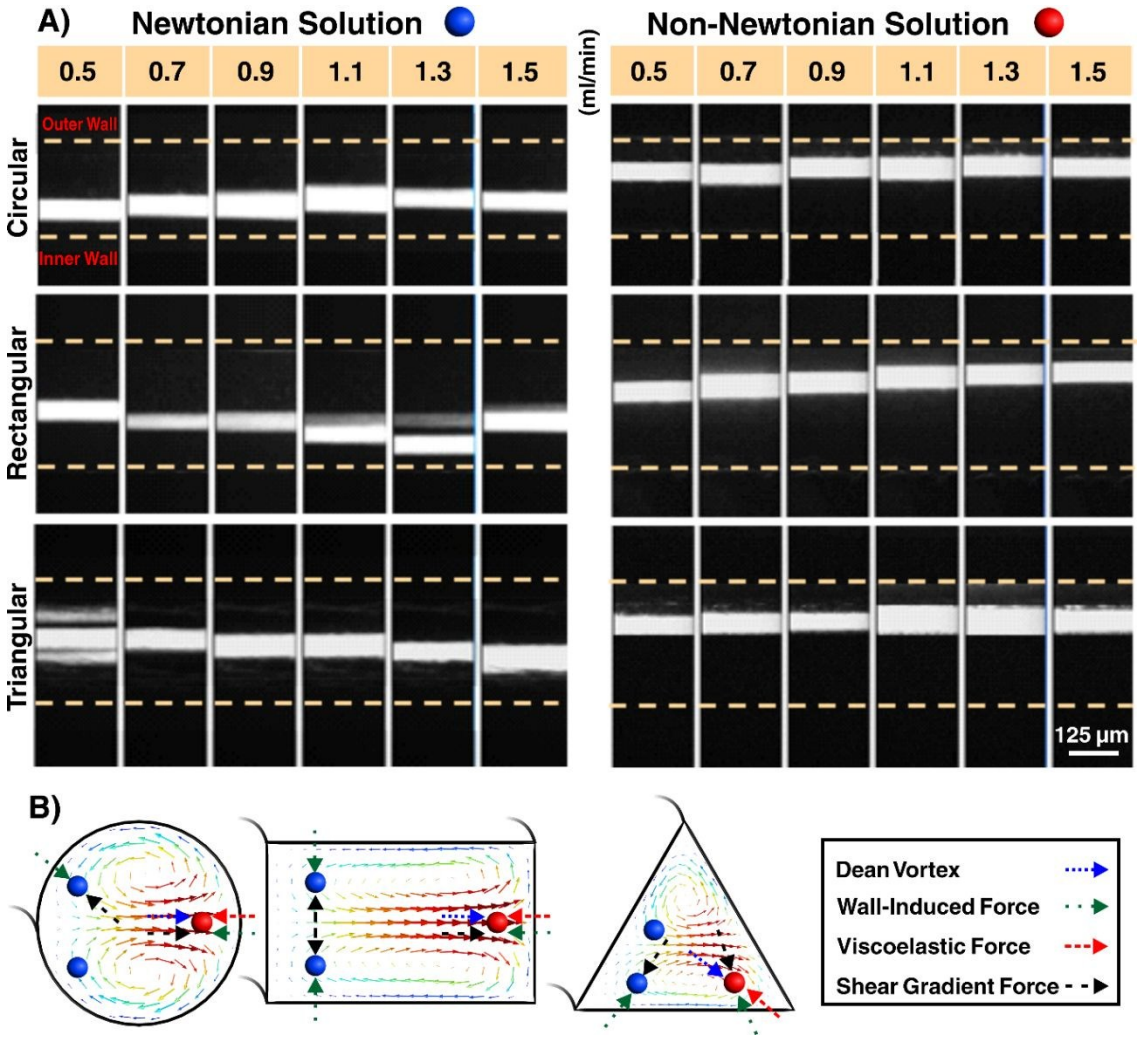

Fig. 4 Focusing of 50 μm particles through circular, rectangular, and triangular curved channels under different flow rates at $\theta = 180^{o}$. A) Fluorescence microscopy results for the Non-Newtonian solution (PEO (2000 ppm)) and Newtonian solution (PBS) which shows a distinct focusing near the outer and inner walls, respectively. B) Cross-sectional view of the channels which shows the Dean vortices, inertial, and elastic lift forces, and the equilibrium positions for the flow rate of 1.1 ml/min.

3.4.2 Straight Channels

Trapezoidal microchannels have recently proved to have higher efficiency and better resolution (i.e., distance between two particle streaks) in particle separation in comparison to conventional microchannels such as rectangular and square channels due to the non-linearity of their cross-section [46].

View Article Online
DOI: 10.1039/C9SM02067E

In this section, the effects of a trapezoidal cross-section on particle migration for Newtonian and non-Newtonian solutions were investigated and then the superposition of two trapezoidal cross-sections to form a complex geometry was evaluated. Fig. 5 shows that in straight channels, focusing happens predominately due to the F_W, F_s, F_E, and F_Ω forces. Fig. 5A illustrates that particles equilibrate near the vertical side for the straight trapezoidal channel in the Newtonian solution at a flow rate of 0.5 ml/min. As can be seen in Fig. 5B, dispersed particles initially migrate laterally towards the focusing line where F_W and F_s balance. Then, particles move vertically towards the equilibrium positions under the effect of F_Ω. By increasing the flow rate, the equilibrium positions migrate towards the slanted wall. This is due to the particles' tendency to migrate to regions where the flow rate is lower, minimising the shear stress and pressure gradient on the particles. Conversely, in the complex channel, the focusing positions diverge into two bands, each located in one trapezoidal section, and remain fixed for all flow rates tested. Although the cross-sectional area of the complex channel is almost twice the size of the single trapezoidal channel, the focusing phenomena are still manifest, which suggests that this method can be used to increase the channel cross-sectional area for high-throughput applications (e.g., sample concentration) without diminishing the inertial forces. Providing dual outlets can thus allow separation of distinct output samples. For non-Newtonian solutions, however, particles concentrate at the channel center for both trapezoidal and complex geometry. This is due to the additional viscoelastic force which is stronger around the walls and pushes the particles towards the channel center (Fig. 5B) where F_E is at its minimum range and can be balanced by the opposing inertial forces. As can be seen in Fig. 5A, while particles find an equilibrium position at the center of the trapezoidal channel for all the given flow rates, for the complex channel, they focus in the narrowed

View Article Online
DOI: 10.1039/C9SM02067E

area between the two trapezoidal geometries. The tight single focusing band shows the potential of the complex channel for flow cytometry applications.

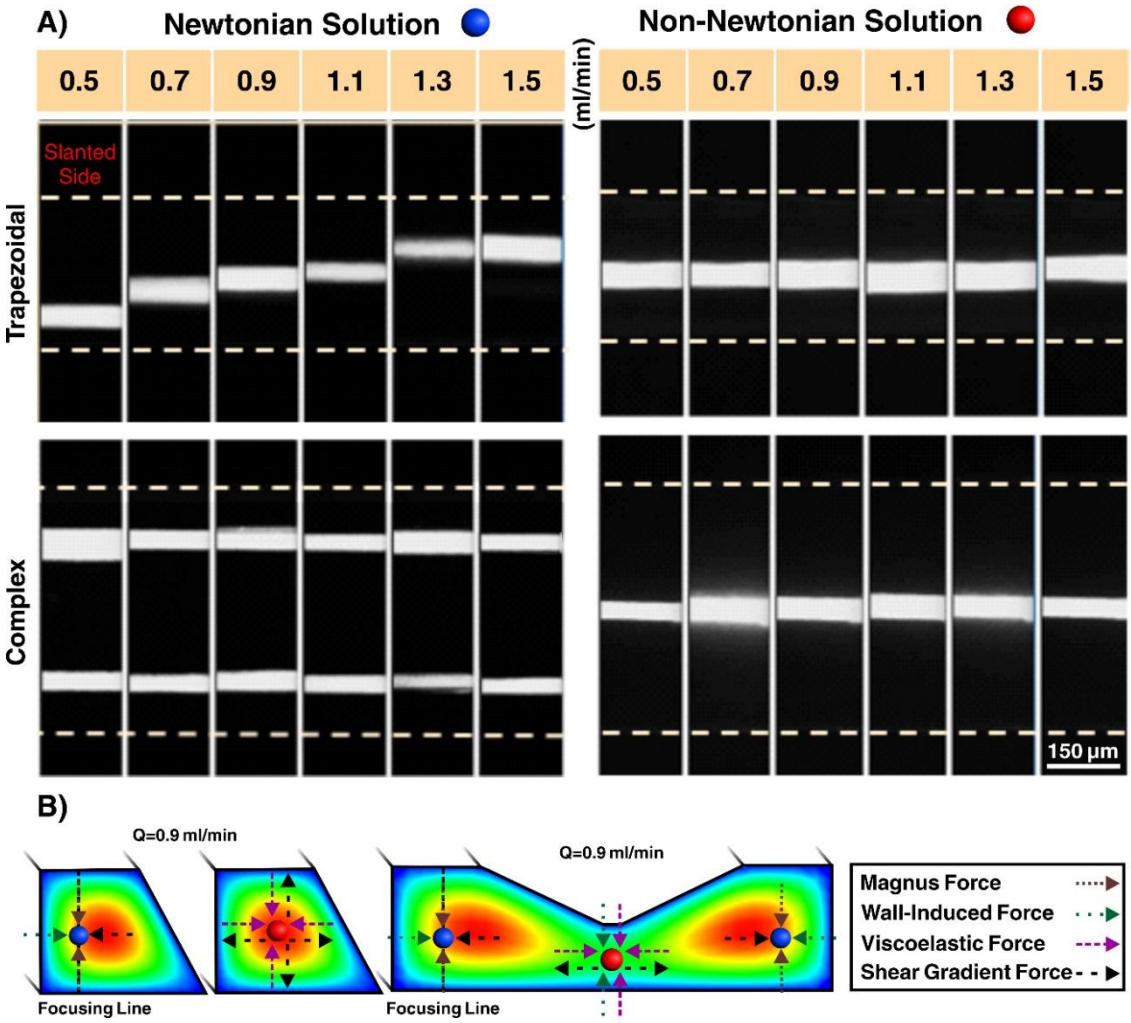

Fig. 5 Focusing of 50 µm particles within straight trapezoidal and complex channels under different flow rates. A) Focusing results for the Non-Newtonian solution (PEO (2000 ppm)) and Newtonian solution (PBS) captured by fluorescence microscopy. For PEO solution, particles focus at the center for all flow rates and channels. However, for the PBS solution and the complex channel, particles focus at both sides for all the flow rates. Equilibrium positions in trapezoidal channel move towards the slanted wall by increasing the flow rates. B) Cross-sectional view of the channels which shows the inertial and elastic forces as well as equilibrium positions for a flow rate of 0.9 ml/min.

View Article Online
DOI: 10.1039/C9SM02067E

3.4.3 Separation of microcarriers from Mesenchymal Stem Cells

Due to the rapid development of cell-based therapy techniques, high-throughput and effective methods are required to grow adherent cell types such as hMSCs. Large-scale manufacturing of stem cells using microcarriers (100–300 μm) in a perfusion bioreactor is proven to be a promising approach; however, downstream separation and purification of the cells from microcarriers has remained a big challenge in the bioprocessing industry [46]. Here, as a proof of concept, a wax-printed spiral complex channel is used to filter microcarriers from the hMSCs (Fig. 6A). To mimic the condition of a bioreactor, a mixture of 180 μm microcarriers and hMSCs (15~30 μm) were prepared in a PBS solution and then pumped into the spiral channel by a peristaltic pump at flow rate of 10 ml/min. To prevent sedimentation of the microcarriers, the suspension was continuously mixed by a stirrer during the experiment. Throughout the channel, cells and microcarriers are affected by the secondary forces and rotate with the secondary flows. After 4 loops, microcarriers focus on the inner side of the channel, where Dean drag and inertial forces balance each other. However, stem cells remain dispersed because the blockage ratio for stem cells is smaller than 0.06; hence, the effect of inertial forces on them is negligible. (Please refer to movie S1 in electronic supplementary information (ESI)). Fig. 6B I and 6B II show the microcarriers collected from the inner outlet and the stem cells harvested from the outer outlet after the second pass, respectively. The microcarrier separation efficiency and the cell recovery rate were approximately 98% and 93%, respectively, demonstrating the ability of the complex spiral channel to fractionate microcarriers and cells effectively. Also, the cell viability was maintained more than 90% for both outlets; 94.2% ± 1.3 for the outlet dedicated to the inner wall and 95.6 ± 1.8 for the outlet dedicated to the outer wall. The harvested cells were cultured in a plastic tissue culture and formed a cell monolayer within 3 days, confirming their viability for downstream assays (Fig. 6B III). Besides, multipotency test was performed to evaluate the quality of the stem cells for differentiating into

View Article Online
DOI: 10.1039/C9SM02067E

osteoblasts, adipocytes, and chondrocytes. The results demonstrated that the multipotency of the collected hMSCs was totally retained and not compromised.

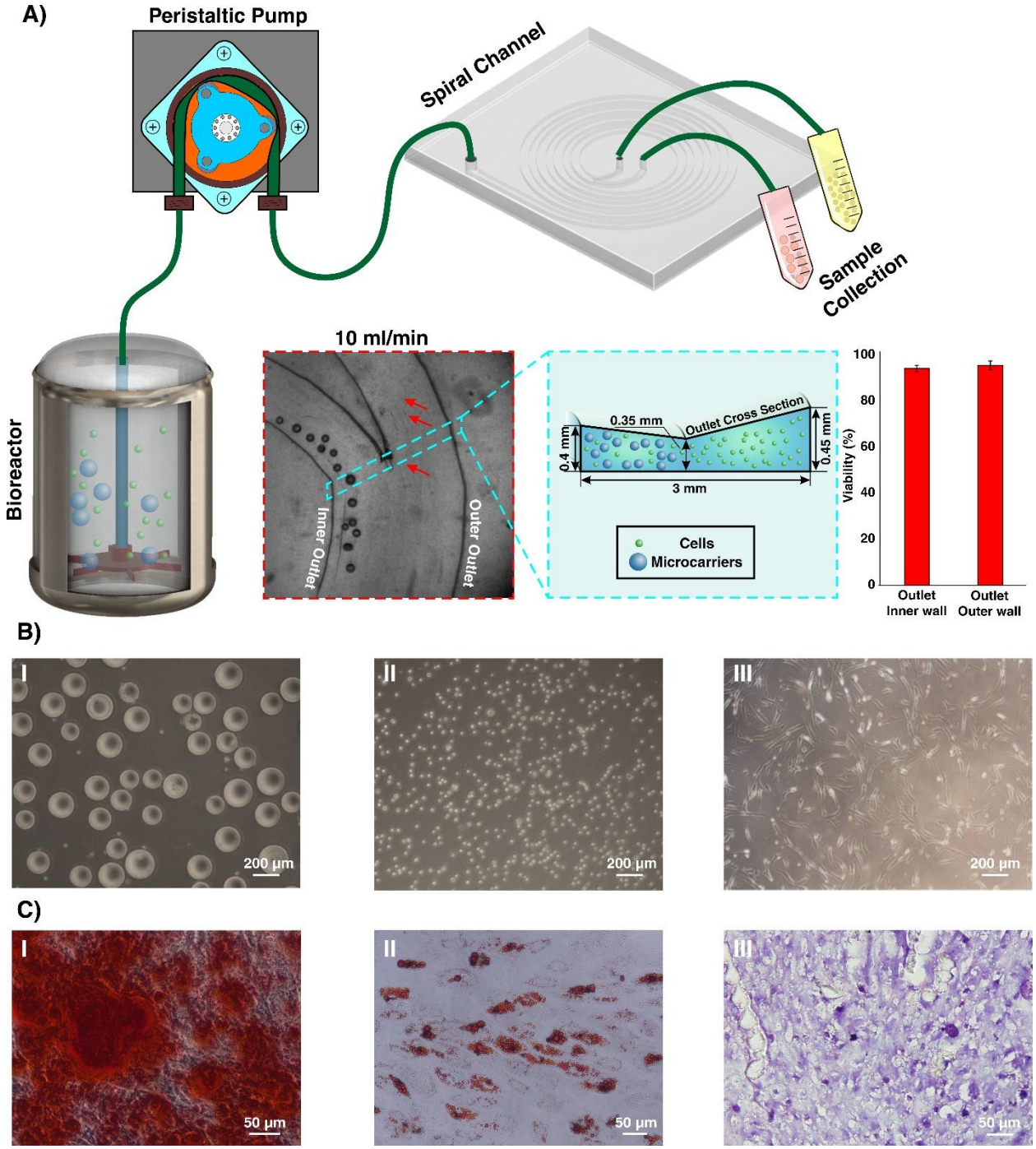

Fig. 6 Microcarrier separation from stem cell suspensions. A) Schematic model of the setup which shows the suspension in a bioreactor injected into the microchannel at 10 ml/min by a peristaltic pump. Channel dimensions are illustrated as inset in the figure. Before the bifurcation, microcarriers migrate to the inner wall and can be extracted there. Red arrows indicate the cells

View Article Online
DOI: 10.1039/C9SM02067E

flowing through the outer outlet. The cell viability was maintained more than 90% for both outlets. B Ⅰ) Collected microcarriers from the outer outlet. B ⅠI) Harvested stem cells from the inner outlet after the second pass. B ⅠII) stem cell monolayer formation after 3 days. C) Multipotency assay of collected hMSCs stained by Alizarin red, Oil Red O, and Alcian blue to demonstrate I) Osteogenic, II) Adpogenic, and III) Chondrogenic differentiation, respectively.

Trilineage differentiation into osteogenic, chondrogenic, and adipogenic lineages after 28 days showed that staining was positive for the 3 differentiated lineages, as shown in Fig. 6C. Lipid vacuole formation was visualized using Oil Red O which confirmed adipocytic phenotype (Fig. 6C II). Glycosaminoglycan complex stained by Alcian Blue showed chondrocytic phenotype (Fig. 6C III), and positive staining of the mineralized matrix by Alizarin Red S demonstrated osteoblastic phenotype (Fig. 6C I).

4 Conclusion

In this paper, a high-quality wax 3D printer and softlithograghy through a novel workflow is employed to eliminate the need for the use of harsh chemicals, multiple cleaning steps, and more importantly PDMS bonding in most conventional methods. We have shown that by adding dummy structures to reinforce the template and dissolving the support wax on a PDMS slab to eliminate the additional handling steps, one can make various microfluidic microchannels with any arbitrary cross-section. Careful characterization of fabricated microchannels using this approach revealed that all geometries have a good surface finish with Sa of ~ 1.75, reproducing the intended design with dimension errors of less than 3%.

In addition, focusing of 50 μm particles in Newtonian and non-Newtonian solutions, for various curved and straight channels was demonstrated to highlight the suitability of this technique for inertial microfluidics. Systematic analysis of curved microchannels using numerical simulations revealed that rectangular-shape channels have lower helicity values compared to the

View Article Online
DOI: 10.1039/C9SM02067E

circular and triangular geometries at similar flow rates. As such, for high-throughput focusing applications, a rectangular channel is preferable, as it has lower helicity values and consequently less particle mixing. As expected, experimental results revealed that the focusing positions in Newtonian and non-Newtonian solutions are quite different, due to the extra viscoelastic force applied on the particles. For the Newtonian solutions, particles find equilibrium close to the inner wall of the curved channels, while for the non-Newtonian solutions, equilibrium positions move towards the outer wall due to viscoelastic force. In straight channels, for a trapezoidal shape and Newtonian solution, increasing the flow rates resulted in a migration of the focusing line from the vertical side to the slanted side. However, for the non-Newtonian solution, particles focused at the center of the channel for all the tested flow rates. While the cross-sectional area of the complex channel is almost twice the size of the single trapezoidal channel, distinct focusing in the complex channel showed the potential of the superposition technique for high-throughput applications. Finally, as a proof of concept, we fabricated a spiral channel with a maximum cell-holding capacity able to separate microcarriers from MSCs with over 98% efficiency. We believe this new method for fabrication of complex inertial microfluidic channels will open up avenues for researchers to explore new physics and develop new applications for the promising field of microfluidics.

5 Acknowledgment

This research work is supported by the Australian Research Council through discovery project grants (DP170103704 and DP180103003) and the National Health and Medical Research Council via the Career Development Fellowship (APP1143377).

References

1. J. Zhang, S. Yan, D. Yuan, G. Alici, N.-T. Nguyen, M. E. Warkiani and W. Li, *Lab on a Chip*, 2016, **16**, 10-34.
2. G. Segre, *Nature*, 1961, **189**, 209-210.

View Article Online
DOI: 10.1039/C9SM02067E

3. J. B. McLaughlin, *Journal of Fluid Mechanics*, 1993, **246**, 249-265.
4. E. S. Asmolov, *Journal of Fluid Mechanics*, 1999, **381**, 63-87.
5. D. D. Joseph and D. Ocando, *Journal of Fluid Mechanics*, 2002, **454**.
6. D. Jiang, W. Tang, N. Xiang and Z. Ni, *RSC Advances*, 2016, **6**, 57647-57657.
7. A. Volpe, P. Paiè, A. Ancona, R. Osellame, P. M. Lugarà and G. Pascazio, *Journal of Physics D: Applied Physics*, 2017, **50**.
8. A. A. S. Bhagat, S. S. Kuntaegowdanahalli and I. Papautsky, *Physics of Fluids*, 2008, **20**.
9. M. A. Faridi, H. Ramachandraiah, I. Banerjee, S. Ardabili, S. Zelenin and A. Russom, *J Nanobiotechnology*, 2017, **15**, 3.
10. A. Lashkaripour, A. A. Mehrizi, M. Goharimanesh, M. Rasouli and S. R. Bazaz, *Journal of Mechanics in Medicine and Biology*, 2018, 1850002.
11. A. A. S. Bhagat, S. S. Kuntaegowdanahalli, N. Kaval, C. J. Seliskar and I. Papautsky, *Biomed. Microdevices*, 2010, **12**, 187-195.
12. A. J. Chung, D. Pulido, J. C. Oka, H. Amini, M. Masaeli and D. Di Carlo, *Lab on a Chip*, 2013, **13**, 2942-2949.
13. M. Rafeie, M. Welleweerd, A. Hassanzadeh-Barforoushi, M. Asadnia, W. Olthuis and M. Ebrahimi Warkiani, *Biomicrofluidics*, 2017, **11**, 014108.
14. M. Rasouli, A. A. Mehrizi, M. Goharimanesh, A. Lashkaripour and S. R. Bazaz, *Chemical Engineering and Processing-Process Intensification*, 2018.
15. H. W. Hou, M. E. Warkiani, B. L. Khoo, Z. R. Li, R. A. Soo, D. S.-W. Tan, W.-T. Lim, J. Han, A. A. S. Bhagat and C. T. Lim, *Scientific reports*, 2013, **3**, 1259.
16. J. Zhou, P. V. Giridhar, S. Kasper and I. Papautsky, *Lab on a Chip*, 2013, **13**, 1919-1929.
17. M. E. Warkiani, A. K. P. Tay, B. L. Khoo, X. Xiaofeng, J. Han and C. T. Lim, *Lab on a Chip*, 2015, **15**, 1101-1109.
18. A. Kulasinghe, T. H. P. Tran, T. Blick, K. O'Byrne, E. W. Thompson, M. E. Warkiani, C. Nelson, L. Kenny and C. Punyadeera, *Scientific Reports*, 2017, **7**, 42517.
19. H. Amini, E. Sollier, M. Masaeli, Y. Xie, B. Ganapathysubramanian, H. A. Stone and D. Di Carlo, *Nat Commun*, 2013, **4**, 1826.
20. M. Jimenez, B. Miller and H. L. Bridle, *Chemical Engineering Science*, 2017, **157**, 247-254.
21. T. Kwon, H. Prentice, J. D. Oliveira, N. Madziva, M. E. Warkiani, J.-F. P. Hamel and J. Han, *Scientific Reports*, 2017, **7**, 6703.
22. M. R. Condina, B. A. Dilmetz, S. Razavi Bazaz, J. Meneses, M. Ebrahimi Warkiani and P. Hoffmann, *Lab on a Chip*, 2019, **19**, 1961-1970.
23. J. A. Kim, J. R. Lee, T. J. Je, E. C. Jeon and W. Lee, *Anal Chem*, 2018, **90**, 1827-1835.
24. Y. Zhang, H. Jing, K. Xu, C. Gao, Y. Hao, F. Meng, Y. Gui and G. Chen, 2017.
25. L.-L. Fan, Q. Yan, J. Guo, H. Zhao, L. Zhao and J. Zhe, *Journal of Micromechanics and Microengineering*, 2016, **27**, 015027.
26. J.-A. Kim, J. Lee, C. Wu, S. Nam, D. Di Carlo and W. Lee, *Lab on a Chip*, 2016, **16**, 992-1001.
27. L.-L. Fan, Q. Yan, J. Zhe and L. Zhao, *Journal of Micromechanics and Microengineering*, 2018, **28**, 065011.
28. H. N. Chan, Y. Chen, Y. Shu, Y. Chen, Q. Tian and H. Wu, *Microfluidics and Nanofluidics*, 2015, **19**, 9-18.
29. S. R. Bazaz, A. A. Mehrizi, S. Ghorbani, S. Vasilescu, M. Asadnia and M. E. Warkiani, *RSC Advances*, 2018, **8**, 33103-33120.
30. B. Bohl, R. Steger, R. Zengerle and P. Koltay, *Journal of micromechanics and microengineering*, 2005, **15**, 1125.
31. S. S. Kuntaegowdanahalli, A. A. S. Bhagat, G. Kumar and I. Papautsky, *Lab on a Chip*, 2009, **9**, 2973-2980.
32. M. G. Lee, J. H. Shin, C. Y. Bae, S. Choi and J.-K. Park, *Anal. Chem.*, 2013, **85**, 6213-6218.
33. M. E. Warkiani, B. L. Khoo, D. S.-W. Tan, A. A. S. Bhagat, W.-T. Lim, Y. S. Yap, S. C. Lee, R. A. Soo, J. Han and C. T. Lim, *Analyst*, 2014, **139**, 3245-3255.

View Article Online
DOI: 10.1039/C9SM02067E

34. J. Hansson, J. M. Karlsson, T. Haraldsson, H. Brismar, W. van der Wijngaart and A. Russom, *Lab on a Chip*, 2012, **12**, 4644-4650.
35. N. Xiang and Z. Ni, *Biomedical Microdevices*, 2015, **17**, 110.
36. P. Yager, T. Edwards, E. Fu, K. Helton, K. Nelson, M. R. Tam and B. H. Weigl, *Nature*, 2006, **442**, 412-418.
37. G. M. Whitesides, E. Ostuni, S. Takayama, X. Jiang and D. E. Ingber, *Annu Rev Biomed Eng*, 2001, **3**, 335-373.
38. M. Abdelgawad, M. W. Watson, E. W. Young, J. M. Mudrik, M. D. Ungrin and A. R. Wheeler, *Lab on a Chip*, 2008, **8**, 1379-1385.
39. D.-K. Lee, J. Y. Kwon and Y. H. Cho, *Applied Physics A*, 2019, **125**, 291.
40. M. A. Raoufi, A. Mashhadian, H. Niazmand, M. Asadnia, A. Razmjou and M. E. Warkiani, *Biomicrofluidics*, 2019, **13**, 034103.
41. P. Mukherjee, X. Wang, J. Zhou and I. Papautsky, *Lab on a Chip*, 2019, **19**, 147-157.
42. S. Zeinali, B. Cetin, S. N. B. Oliaei and Y. Karpat, *Electrophoresis*, 2015, **36**, 1432-1442.
43. Y.-C. Lin, C.-C. Lee, H.-S. Lin, Z.-H. Hong, F.-C. Hsu, T.-P. Hung and Y.-T. Lyu, *Microsystem Technologies*, 2017, **23**, 1661-1669.
44. A. Lashkaripour, R. Silva and D. Densmore, *Microfluidics and Nanofluidics*, 2018, **22**, 31.
45. M. E. Warkiani, G. Guan, K. B. Luan, W. C. Lee, A. A. S. Bhagat, P. K. Chaudhuri, D. S.-W. Tan, W. T. Lim, S. C. Lee and P. C. Chen, *Lab on a Chip*, 2014, **14**, 128-137.
46. R. Moloudi, S. Oh, C. Yang, M. Ebrahimi Warkiani and M. W. Naing, *Microfluidics and Nanofluidics*, 2018, **22**, 33.
47. Y. He, W. Wu, T. Zhang and J. Fu, *RSC Advances*, 2015, **5**, 39138-39144.
48. X. Wang, C. Liedert, R. Liedert and I. Papautsky, *Lab Chip*, 2016, **16**, 1821-1830.
49. Y. Liao, Y. Ju, L. Zhang, F. He, Q. Zhang, Y. Shen, D. Chen, Y. Cheng, Z. Xu, K. Sugioka and K. Midorikawa, *Opt Lett*, 2010, **35**, 3225-3227.
50. P. Paiè, F. Bragheri, D. Di Carlo and R. Osellame, *Microsystems & Nanoengineering*, 2017, **3**, 17027.
51. B. Miller, M. Jimenez and H. Bridle, *Scientific Reports*, 2016, **6**, 36386.
52. Y.-S. Lee, N. Bhattacharjee and A. Folch, *Lab on a Chip*, 2018, **18**, 1207-1214.
53. A. Naderi, N. Bhattacharjee and A. Folch, *Annual Review of Biomedical Engineering*, 2019, **21**, 325-364.
54. A. K. Au, N. Bhattacharjee, L. F. Horowitz, T. C. Chang and A. Folch, *Lab on a Chip*, 2015, **15**, 1934-1941.
55. A. K. Au, W. Huynh, L. F. Horowitz and A. Folch, *Angew Chem Int Ed Engl*, 2016, **55**, 3862-3881.
56. N. Bhattacharjee, C. Parra-Cabrera, Y. T. Kim, A. P. Kuo and A. Folch, *Adv. Mater.*, 2018, **30**, 1800001.
57. W. Lee, D. Kwon, W. Choi, G. Y. Jung, A. K. Au, A. Folch and S. Jeon, *Scientific reports*, 2015, **5**, 7717.
58. C. I. Rogers, K. Qaderi, A. T. Woolley and G. P. Nordin, *Biomicrofluidics*, 2015, **9**, 016501.
59. H. Gong, A. T. Woolley and G. P. Nordin, *Lab on a Chip*, 2016, **16**, 2450-2458.
60. H. Gong, B. P. Bickham, A. T. Woolley and G. P. Nordin, *Lab on a Chip*, 2017, **17**, 2899-2909.
61. A. Urrios, C. Parra-Cabrera, N. Bhattacharjee, A. M. Gonzalez-Suarez, L. G. Rigat-Brugarolas, U. Nallapatti, J. Samitier, C. A. DeForest, F. Posas and J. L. Garcia-Cordero, *Lab on a Chip*, 2016, **16**, 2287-2294.
62. M. K. Gelber and R. J. L. o. a. C. Bhargava, 2015, **15**, 1736-1741.
63. S. Mohanty, L. B. Larsen, J. Trifol, P. Szabo, H. V. R. Burri, C. Canali, M. Dufva, J. Emnéus, A. J. M. s. Wolff and e. C, 2015, **55**, 569-578.
64. J.-S. Lee, J. M. Hong, J. W. Jung, J.-H. Shim, J.-H. Oh and D.-W. J. B. Cho, 2014, **6**, 024103.
65. V. Saggiomo and A. H. Velders, 2015, **2**, 1500125.

View Article Online
DOI: 10.1039/C9SM02067E

66. D. P. Parekh, C. Ladd, L. Panich, K. Moussa and M. D. Dickey, *Lab on a Chip*, 2016, **16**, 1812-1820.
67. W. Tang, N. Fan, J. Yang, Z. Li, L. Zhu, D. Jiang, J. Shi and N. Xiang, *Microfluidics and Nanofluidics*, 2019, **23**, 42.
68. K. Kang, S. Oh, H. Yi, S. Han and Y. Hwang, *Biomicrofluidics*, 2018, **12**, 014105.
69. S. Razavi Bazaz, N. Kashaninejad, S. Azadi, K. Patel, M. Asadnia, D. Jin and M. Ebrahimi Warkiani, *Advanced Materials Technologies*, 2019, **4**, 1900425.
70. Z. a. Li, J. Yang, K. Li, L. Zhu and W. Tang, *RSC Advances*, 2017, **7**, 3313-3320.
71. D. Serre, *Comptes Rendus Mécanique*, 2018, **346**, 175-183.
72. A. Russom, A. K. Gupta, S. Nagrath, D. D. Carlo, J. F. Edd and M. Toner, *New Journal of Physics*, 2009, **11**, 075025.
73. D. Di Carlo, D. Irimia, R. G. Tompkins and M. Toner, *Proceedings of the National Academy of Sciences*, 2007, **104**, 18892-18897.
74. S. Ardabili, J. Gantelius, J. Kowalewski, H. Brismar and A. Russom, 2010.
75. J. Zhou and I. Papautsky, *Lab on a Chip*, 2013, **13**, 1121-1132.

View Article Online
DOI: 10.1039/C9SM02067E

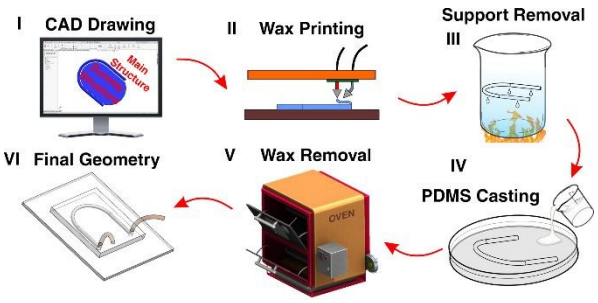

ToC: A novel workflow for the fabrication of inertial microfluidic devices based on the wax 3D printing method